Interpretation of vacancy migration, trapping, and clustering in fcc metals as observed through perturbed angular correlations and distributions of γ rays

Frits Pleiter
Laboratorium voor Algemene Natuurkunde, Rijksuniversiteit Groningen, The Netherlands

Christoph Hohenemser
Department of Physics, Clark University, Worcester, Massachusetts 01610
(Received 10 July 1981)

In the past six years perturbed angular correlations (PAC) and perturbed angular distribution (PAD) of γ rays have been widely applied to study the migration, trapping, and clustering of lattice defects in metals. Essential features of these experiments are distinctive precessional signals arising in the nuclear hyperfine interaction. These signals serve as convenient labels for specific lattice defects bound to γ-ray-emitting probe atoms, and under favorable circumstances provide information on the lattice symmetry of the defects. Because we believe that the maximum information is obtained from such experiments if systematic comparisons are made between similar metals, we describe here our survey and interpretation of PAC and PAD data for seven fcc metals (Ag, Al, Au, Cu, Ni, Pd, Pt) using ^{111}Cd probe. We consider defect production by irradiation, quenching, and ion-implantation, and note that the same defect types recur in all three methods. We include a total of 19 distinctive states in our discussion, and through a series of independent, comparative observations we argue that these states involve vacancy defects bound to the ^{111}Cd probe. On the basis of the observed frequencies, annealing behavior, and electric-field-gradient symmetry we divide vacancy states into four classes. For three of these classes structural assignments can be made. These include the nearest-neighbor monovacancy observed in five metals, divacancies or faulted loops in the {111} plane observed in six metals, and a tetrahedral cluster seen only in Ni. For the nearest-neighbor monovacancy the data permit estimation of migration enthalpies. For the monovacancy the data also permit an interpretation of the observed electric field gradients. Though some of the observed states remain with undetermined structure, we believe our comparative analysis provides an excellent foundation for further detailed study of small vacancy clusters under a variety of metallurgical conditions.

I. INTRODUCTION

Metals contain elementary or point defects such as vacancies and interstitials. Under suitable conditions these combine to form larger defects such as dislocations, loops, and clusters consisting of numerous elementary defects. The study of elementary point defects, their production, migration, agglomeration, and trapping at sinks has been the object of extensive experimental and theoretical work described in recent international conferences.[1–3] The study of larger defects has been of interest wherever technologists have been concerned with work-hardened, temperature-shocked, or irradiated metals.[4,5]

To a considerable extent measurements on point defects have been made by observing thermal annealing of residual resistivity. The method works because it is sensitive to the aggregate concentration of vacancies and interstitials. It is attractive because it is widely applicable and relatively simple. Through a large number of systematic experiments it has produced a model of resistivity recovery that defines a common language for all point-defect research. The five principal stages of the model, as described in recent reviews by Schilling,[6,7] are summarized in Table I. As an aid in visualization of the processes mentioned in Table I, the resistivity recovery of high-purity Cu is illustrated in Fig. 1.[8] Our simplified description of the five stages of recovery does not take into account the interaction of interstitials and vacancies with impurities. Such interaction can grossly alter the behavior seen in stages II and IV, and can lead to the suppression of stage III.

Present understanding of recovery is best for stage I, where for several cases it has been possible to explain quantitatively the details of annealing curves by using only a few variables, such as the defect-activation energy, the defect concentration, and absolute temperature.[9] This kind of program fails for higher stages, particularly stages II and IV, theoretically because aggregation phenomena are more complex than the processes of stage I, and experimentally

TABLE I. Recovery model for resistivity in metals.

Annealing stage	Temperature (expressed as fraction of melting point)	Description
I_A–I_D	0.02	Recombination of close interstitial-vacancy pairs.
I_E	0.025	Free migration of interstitials, followed by formation of interstitial clusters.
II	0.02–0.2	Growth of interstitial clusters, leading eventually to loops that are visible via direct observation methods.
III	0.12–0.2	Free migration of mono- or di-vacancies, leading to annihilation at interstitial clusters, and to formation of vacancy clusters.
IV	0.12–0.4	Growth of vacancy clusters.
V	0.5	Dissociation of remaining interstitial and vacancy clusters, removal of most remaining defects.

because there is at present no generally applicable method with which to monitor the growth of small clusters of individual defects before they become visible in an electron microscope.

A particular problem arises out of the fact that in resistivity-recovery experiments and other similar techniques, the behavior of defects is defined solely in terms of the recovery phenomenon, i.e., there is no specific information which characterizes the structure of the defect responsible for a given annealing stage. To overcome this problem, a number of approaches have been developed which "flag" a particular defect structure via a characteristic signal or "fingerprint." With some notable exceptions these fingerprints do not solve the problem of structure, but permit discrimination between structures. In analogy to the view from Plato's cave, they give the events outside the cave a distinctive shape, but are generally unable to lead to a full description without the intervention of extensive theorizing.

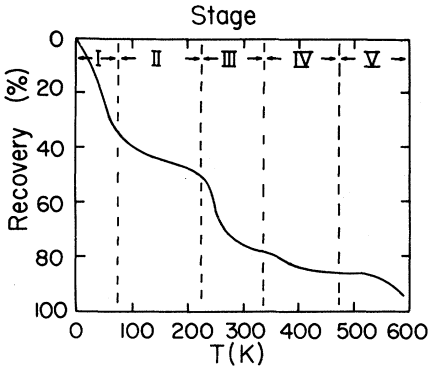

FIG. 1. Resistivity recovery of high-purity Cu after neutron irradiation at low temperature (see, e.g., Ref. 8). In such measurements, the sample is successively raised to the annealing temperature T for fixed periods of about 15 min and then cooled to 4 K for resistivity measurements. The ranges of the traditional five recovery stages are indicated (top).

Seven examples of "structure-specific" methods are summarized in Table II. These include techniques uniquely applicable to interstitials, to vacancies, to lattice location, and to small vacancy clusters.

In this paper we focus on hyperfine interactions, the most recent addition to Table II. Application of hyperfine interactions to lattice defects has been broadly treated in a recent summer school.[10] This showed that hyperfine interactions may offer in certain instances specific information with a resolution that is achieved in few other structure-specific methods. For example, in cubic metals it is routinely possible to "flag" defect-impurity bound states with quadrupole interaction frequencies having a precision of a few percent. This permits quite sensitive distinctions between a range of defect structures.

So far, as results of hyperfine defect spectroscopy have accumulated, there have been few attempts to interpret the numerous signals and annealing patterns

TABLE II. Structure-specific methods of investigation of lattice defects.

Methods	Application to	Limitations
Mechanical relaxation	Vacancies and interstitials	Requires single crystals; yields incomplete microscopic specifications of structure
Diffuse x ray scattering	Mainly interstitials	Requires single crystals; needs detailed theoretical models
Electron microscopy	Vacancy and interstitial clusters, loops	Applies only to larger defects with dimensions larger than ~10 Å
Field ion microscopy	Vacancies and interstitials	Requires high melting metals (e.g., W)
Channeling	Lattice location of interstitial impurities and defects bound to them	Requires single crystals; analysis is difficult except for simple geometries
Positron annihilation	Vacancies and small vacancy clusters	Distinguishes the number of vacancies per defect; is not sensitive to defect geometry
Hyperfine interactions	Impurity-defect bound states for small defects	Provides unique "flags" of defects; quantitative interpretation of data in terms of structure is difficult

in a systematic way. Instead, most authors have limited themselves to discussing the possible interpretations of their own data. Because we think that much can be learned from a comparative discussion of the results now available, we consider here experiments done in face-centered cubic metals using the ^{111}Cd impurity probe. The restriction to data on fcc metals and ^{111}Cd is not as severe as it might seem, because these data constitute the only body of work that is large enough to permit systematic comparisons.

The scope of our comparative discussion includes about 20 bound states with well defined frequencies, occurring in Ag, Al, Au, Cu, Ni, Pd, and Pt.

II. PERTURBED ANGULAR CORRELATION AND DISTRIBUTION OF γ RAYS

Before considering specific results, we describe in heuristic terms the essential features of experimental methods used, i.e., perturbed angular correlation and distribution of γ rays. For a more complete treatment of nuclear radiations, their correlations, distributions, and extra-nuclear perturbations, we refer the reader to a recent treatise edited by Hamilton,[11] or to the article by Frauenfelder and Steffen.[12]

Basic to all methods of interest here is the preparation or selection of an ensemble of excited nuclei with unequal populations of magnetic substates. As such states decay, the probability for γ-ray emission will have an anisotropic distribution with respect to the axis of quantization. In the absence of hyperfine interactions, the directional distribution of the γ rays will be given by

$$W(\theta) = 1 + A_2 P_2(\cos\theta) + \cdots , \quad (1)$$

where the ellipsis indicates higher-order terms and θ is the angle between the axis of quantization and the emitted γ quantum. The anisotropy coefficient A_2 depends on the population imbalance among the magnetic substates and the multipolarity of the emitted γ ray. Neglect of higher-order terms is justified by the relative size of these terms, e.g., for the ^{111}Cd cascade we discuss, $A_4/A_2 < 0.01$.

In the presence of hyperfine interactions, the directional distribution becomes time dependent with the

form

$$W(\theta,t)=1+A_2\hat{G}_2(\theta,t)+\cdots \quad . \tag{2}$$

The function $\hat{G}_2(\theta,t)$ contains all relevant information about the interaction of nuclear moments with extra-nuclear fields, including the possible effects of lattice defects that are the focus of the present paper. It is, therefore, the goal of experiments to measure $\hat{G}_2(\theta,t)$, and to interpret it in terms of the hyperfine interactions that underly it.

One specific case frequently encountered in defect studies is perturbation due to an electric quadrupole interaction with axial symmetry and random orientation. For the $I=\frac{5}{2}$ state of ^{111}Cd we have in this case

$$\hat{G}_2(\theta,t)=G_2(t)P_2(\cos\theta) \quad , \tag{3}$$

$$G_2(t)=\tfrac{1}{5}(1+\tfrac{13}{7}\cos\omega_0 t+\tfrac{10}{7}\cos 2\omega_0 t+\tfrac{5}{7}\cos 3\omega_0 t) \quad , \tag{4}$$

with $\omega_0=(3\pi/10)eQV_{zz}/h$. Here, Q is the nuclear electric quadrupole moment, and V_{zz} is the z component of the diagonalized electric-field-gradient (EFG) tensor.

Another case commonly encountered in defect studies is the case of a magnetic hyperfine field, $H_{\rm hf}$, perpendicular to the directions that define the angle θ. In this case

$$\hat{G}_2(\theta,t)=P_2(\cos(\theta-\omega_L t)) \quad , \tag{5}$$

with $\hbar\omega_L=\mu H_{\rm hf}/I$. Here, μ is the nuclear magnetic dipole moment, and I is the nuclear spin.

To select or produce unequal populations of m states required for these effects, two methods have been used. The first, known as perturbed angular correlations (PAC), is based on a coincidence measurement made on a γ-γ cascade. Detecting the first γ ray in a given direction selects a preferred nuclear-spin direction, and assures that the second γ ray has an anisotropic distribution. The time-dependent coincidence rate has the form

$$C(\theta,t)=C_0\exp(-t/\tau_N)W(\theta,t) \quad , \tag{6}$$

where τ_N is the mean life of the intermediate nuclear state. In the second method, known as perturbed angular distributions (PAD), the initial unequal population of magnetic substates is established through excitation via a pulsed accelerator beam. In this case, only the decay γ ray is detected and the rate of delayed coincidences between the beam pulse and the γ ray takes the form of Eq. (6).

All the experiments considered here utilize the isotope ^{111}Cd, or its parents ^{111}In and ^{111}Ag. As shown in Fig. 2, the 245-keV state in ^{111}Cd is fed from the ground state of ^{111}In ($T_{1/2}=2.8$ d) and from the ground state of ^{111}Ag ($T_{1/2}=7.5$ d).[13] This state is ideal for several reasons. (1) It is populated and decays via γ rays that are easily detected with high efficiency and good time resolution. (2) The involved anisotropies are relatively large, viz., $A_2=-0.17$ for the 171–245-keV γ-ray cascade, $A_2\approx-0.14$ for the 97–245-keV γ-ray cascade, and, for PAD, $A_2=0.08$–0.12 depending on the nuclear reaction

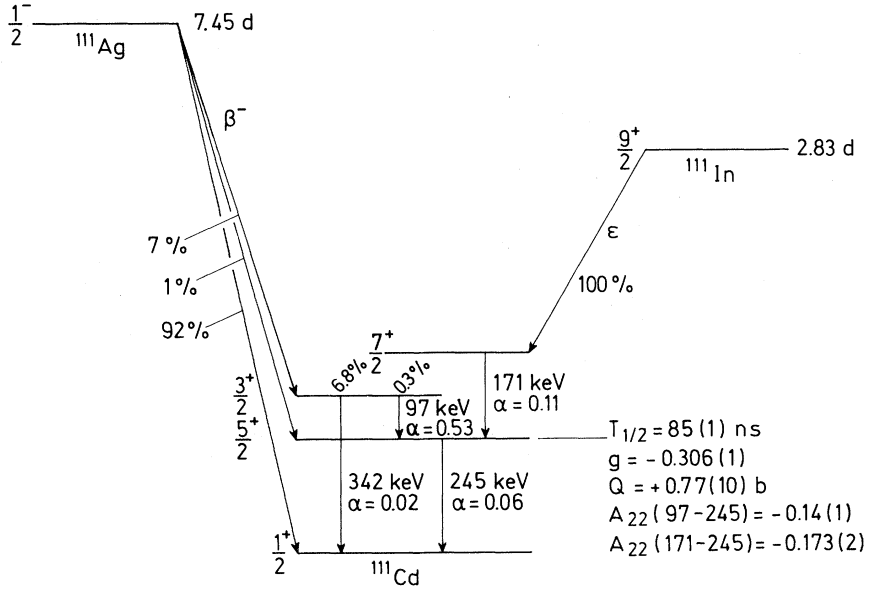

FIG. 2. Partial decay schemes of ^{111}Ag and ^{111}In (from Ref. 13).

employed. (3) Its relatively big nuclear moments, $\mu = -0.765$ nm and $Q = +0.77$ b, make it sensitive to both magnetic and electric hyperfine interactions. (4) Its 85-ns half-life is well matched to a range of hyperfine frequencies encountered in both magnetic and nonmagnetic solids, as well as available electronic timing methods.

III. INTERPRETATION OF DATA

To indicate how information about lattice defects is deduced from PAC and PAD experiments, we consider next some specific aspects of the data.

For PAC and PAD the presence of lattice defects in the close neighborhood of probe atoms is signaled by perturbation factors that differ distinctly from those of an undisturbed lattice. In the case of cubic nonmagnetic metals, ^{111}Cd with a near-neighbor defect shows a discrete electric quadrupole interaction. Because this interaction is zero for undisturbed lattice sites, PAC and PAD offer the possibility of measuring near-neighbor defect states against a zero background from ^{111}Cd in defect-free lattice positions. At the same time, defect sites with cubic symmetry will be "invisible." In the case of magnetic metals, defect sites may be identified via both magnetic dipole and electric quadrupole interactions. In this case cubic sites are visible because they exhibit a magnetic precession frequency. This means that magnetic metals in principle permit detection of all sites, and thus offer richer possibilities than nonmagnetic metals. To illustrate these propositions, we consider two examples from the work of the Groningen group.

^{111}In implanted in platinum. Pleiter *et al.*[14] have implanted ^{111}In into Pt at 10 K, and have measured the perturbation factor of ^{111}Cd after annealing at various higher temperatures. As shown in Fig. 3 (top), right after implantation the perturbation factor exhibits a gradual decrease superposed on a single, discrete electric quadrupole frequency. The former is interpreted as due to weak interactions with distant lattice defects, the later as resulting from ^{111}Cd bound to a near-neighbor defect. The discrete quadrupole frequency serves to "flag" the bound state for identification in subsequent observations. From the amplitude of the observed modulation one may deduce that about 10% of the ^{111}Cd atoms are in the bound state. From the specific form of the modulation one may conclude that the bound state possesses at least a threefold axis of symmetry.

Upon annealing, a much larger frequency appears, indicating that a second distinct bound state has been formed, in this case involving an additional 10% of the ^{111}Cd atoms. Such a state can be formed if lattice defects distant from a given ^{111}In probe atom are thermally activated, migrate through the lattice, and become trapped on the ^{111}In. It can also occur if the

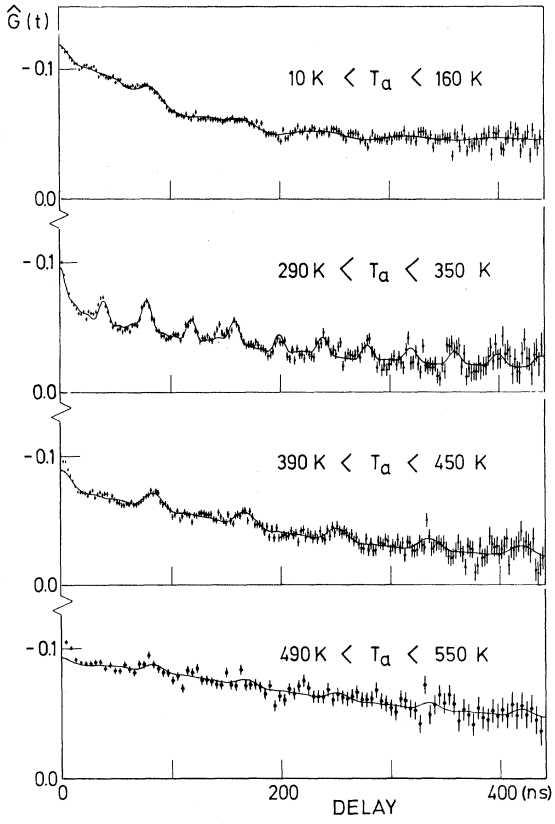

FIG. 3. Perturbation factors for ^{111}In implanted in Pt at 10 K, after annealing at different temperatures T_a. From Pleiter *et al.* (Ref. 14).

^{111}In itself migrates (in this case impossible because of the low annealing temperature involved). When the annealing temperature is further raised the two defect frequencies disappear, the first at 470 K, the second at 380 K. This indicates that the bound states have been broken, or that additional defects are trapped such that ^{111}In with cubic local symmetry remains.

^{111}In implanted in nickel. Hohenemser *et al.*[15] have implanted ^{111}In into Ni at 10 K, and have measured the perturbation factor after annealing at various higher temperatures. Immediately following implantation, the perturbation factor consists of a single precessional signal due to a magnetic hyperfine field of $-7.1\,T$. This is identified as due to ^{111}Cd in an undisturbed lattice because it has the same magnitude as the field determined in diffused, defect-free samples. After annealing at 400 K, two different magnetic frequencies are present, as illustrated in Fig. 4. The larger of these is the field of the undisturbed ^{111}Cd observed at low temperature, and the smaller is assigned to a defect state. Since no detectable quadru-

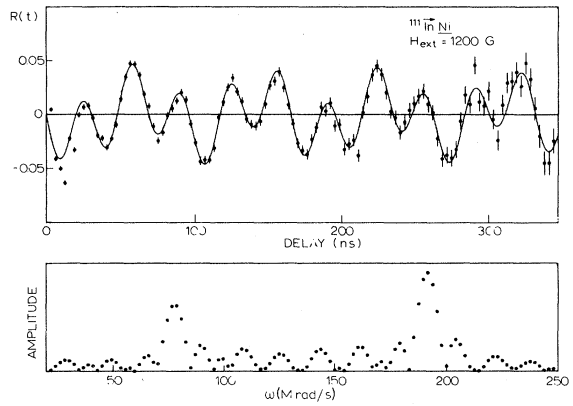

FIG. 4. Perturbation factor for ^{111}In implanted in Ni and its Fourier transform, after annealing at 400 K. Measurement conducted at 300 K. From Hohenemser *et al.* (Ref. 15).

pole perturbation affects the latter, one must conclude that we are dealing with a bound state of cubic symmetry, i.e., one that would not have been seen in a nonmagnetic material.

When measurements are made above the Curie temperature $T_C = 631$ K, all magnetic interactions are turned off, and only noncubic sites are visible through their quadrupole interactions. As shown in Fig. 5 (top) such measurements detect a second defect site in Ni, characterized by an EFG with axial symmetry as in the case of Pt. Below T_C this defect remains present, but because of interference effects produced by the combined electric-magnetic interactions[16] the modulation is less distinct [Fig. 5 (bottom)].

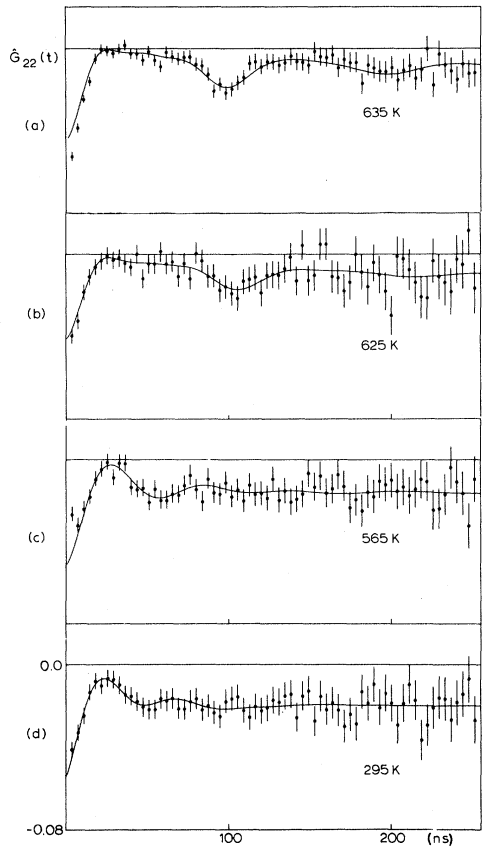

FIG. 5. Perturbation factors for ^{111}In implanted in Ni, after annealing at 640 K. Sample was magnetized in a longitudinal field. Combined magnetic and electric hyperfine interactions were observed below the Curie temperature, $T_C = 631$ K. From Pleiter *et al.* (Ref. 16).

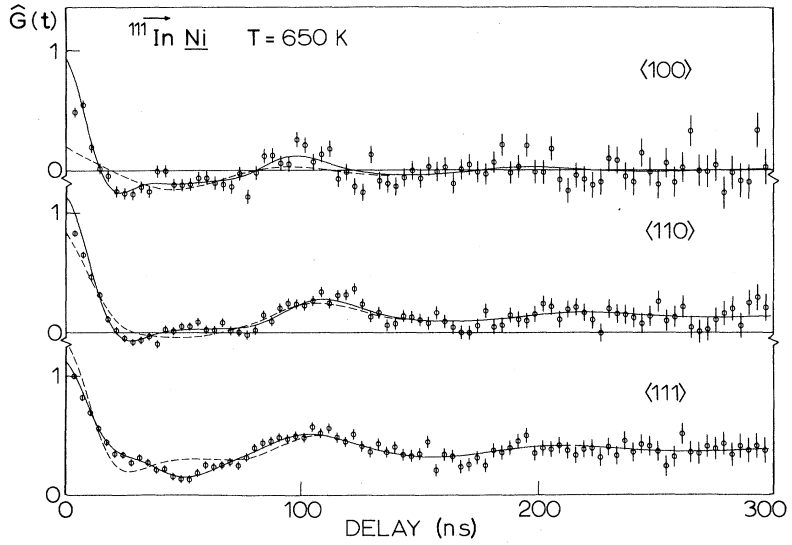

FIG. 6. Perturbation factors for ^{111}In implanted in a single crystal of Ni, measured at 650 K for three different orientations of the γ-ray detectors with respect to the crystallographic axes. Drawn curve: calculated for EFG with principal z axis along ⟨111⟩ crystallographic direction. Dashed curve: calculated for EFG with z axis along ⟨100⟩ direction. From Pleiter (Ref. 17).

For oriented single crystals the details of the modulation pattern depend on the orientation of the EFG principal axes relative to the counter axes. Pleiter[17] has used this fact to deduce the orientation of the principal axes for the noncubic defect visible in Ni above T_C. As illustrated in Fig. 6, he found that the principal z axis points into the $\langle 111 \rangle$ crystallographic direction.

Taken together, our examples show that PAC methods offer a number of independent and quite powerful ways of characterizing probe-defect bound states, defect migration, and defect transformation in cubic metals. In fact, even greater power is available from systematic comparisons of data obtained for different related systems. As a first step in such a comparison, we survey the range of experimental work.

IV. METHODS OF DEFECT PRODUCTION

Lattice defects have been introduced into fcc metals via irradiation, quenching and ion implantation. For all three methods of defect preparation isochronal annealing procedures have been employed. In these procedures, samples are successively heated to a range of annealing temperatures, and remeasured at the temperature at which the defects were first introduced. Thresholds for thermal activation of different frequencies are found, and comparisons to resistivity recovery stages have been made.

As in the examples described in Sec. III, the observed frequencies have been attributed to defects trapped at distinctive lattice locations in the near neighborhood of the probe atom. There are two principal justifications for this interpretation. (1) The observed states appear at a given temperature as a result of thermal activation, and disappear at a higher temperature; because probe atoms are immobile at these temperatures, it may be safely assumed that the defect and not the probe atom moves in forming the trap. (2) The observed frequencies are in most cases found to be sharp rather than distributed. This suggests that the defect is located in a well-defined site in the neighborhood of the probe atom.

The three methods of introducing defects have a number of essential differences, and may be described as follows.

Irradiation. In irradiation experiments, ^{111}In-doped samples are bombarded by electrons or heavier particles. Because defects so formed are randomly distributed with respect to the ^{111}In probe atom, they can be trapped only if, after thermal activation, migrating defects do not get lost at other sinks. Samples should therefore be rather pure. It is remarkable that with ^{111}In concentrations of $\sim$1 ppm or less trapping in irradiated samples has not been a problem. Evidently, ^{111}In has both a large binding energy and an appreciable trapping radius for the defects concerned.

Quenching. In quenching experiments, ^{111}In-doped samples are cooled rapidly from temperatures near the melting point. As in the case of irradiation, the nonequilibrium distribution of vacancies so produced is random with respect to the ^{111}In probe atoms. In addition, however, the defects and probe atoms are mobile during much of the quench, and may form bound states before the final temperature is reached. Thermal activation experiments may fail because all available defects have already trapped or clustered in strongly bound states during cooling. Quenching involves the additional difficulty that migration of the ^{111}In dopant may cause aggregation and/or condensation at grain boundaries and other free surfaces. It is therefore not so surprising that quenching has not been successful in all cases in which it has been tried.

Implantation. In implantation experiments, energetic ^{111}In probe ions are injected into targets of fcc metals. In this case defects are spatially correlated with the position of the implanted ion. For low-dose implantation (nonoverlapping damage cascades) trapped defects are exclusively drawn from the near neighborhood of the stopped ion, with the result that some kinds of defects are favored over others (see Sec. VI). In some cases impurity-defect bonds may already form in the few picoseconds required for the damage cascade to "cool." In other cases, defects from the immediate neighborhood are trapped only after thermal activation.

In the case of ion-beam recoil implantation and mass separator implantation[10] there is sufficient time during the 2.8-d lifetime of ^{111}In to carry out annealing experiments of the usual kind. In the case of in-beam PAD experiments on ^{111}Cd, the available time is limited by the 85-ns half-life of the 245-keV state. The resulting shifts of the recovery stages to higher temperatures have been observed by Bertschat *et al.*[18,19]

V. SURVEY OF EXPERIMENTAL RESULTS

The scope of our comparative discussion is indicated in Table III. The data presented on Ag, Al, Au, Cu, Ni, Pd, and Pt include all of which we are aware, with the exception of a few defect states that could be produced only by low-temperature electron irradiation and apparently have to be associated with trapping of interstitials. As can be seen from Table III, the data are classified according to defect production method, observed frequency, activation temperature, symmetry of the EFG, and crystallographic direction of the EFG principal z axis. In all cases the frequencies are listed as given by the authors.[14–47]

Because Table III obviously involves a number of duplicate listings of defect states, we show in Table IV a reduced list obtained by combining cases that in our judgment refer to the same state. We omitted

TABLE III. Survey of ^{111}Cd defect-associated hyperfine interaction frequencies.

Host	Stage III[a] temperature (K)	Method	Preparation[b] T_{act} (K)	Defects Properties[c] ω_0 (Mrad/s)	η	$\langle \cdots \rangle$	ω_L (Mrad/s)	Authors	References
Ag	240	Im	350	40(8)	0	· · ·	· · ·	Thomé and Bernas	22–24
		Ir,Q	220	34(2)	· · ·	· · ·	· · ·	Butt *et al.*	25
		Im	(80)	85(2)	0	· · ·	· · ·	Thomé and Bernas	22–24
		Ir	220	75(2)	· · ·	· · ·	· · ·	Butt *et al.*	25
		Ir	220	75(2)	0	· · ·	· · ·	Deicher *et al.*	26
		· · ·	· · ·	77	0	⟨110⟩	· · ·	Deicher *et al.*	27
		Im	(300)	157(2)	0	· · ·	· · ·	Behar and Steffen	20,21
Al	220	Im	300	47(1)	<0.2	⟨111⟩	· · ·	Pleiter and Prasad	31
		Ir,Q	200	62(3)	0.41(5)	· · ·	· · ·	Rinneberg *et al.*	28,30
		Im	(80)	60(1)	0.41(2)	· · ·	· · ·	Pleiter and Prasad	31
		Ir,Q	200	125(5)	0.0(1)	· · ·	· · ·	Rinneberg *et al.*	28,29
		Im	(80)	123(1)	<0.1	· · ·	· · ·	Pleiter and Prasad	31
		· · ·	160	124(1)	<0.1	⟨111⟩	· · ·	Müller	32
Au	300	Im,Ir,Q	270	38(1)	0.00(3)	⟨111⟩	· · ·	Deicher *et al.*	33,34
		Ir,Q	240	86(1)	0.00(3)	⟨110⟩	· · ·	Deicher *et al.*	33,34
		Im	(100)	89(4)	0	· · ·	· · ·	Deicher *et al.*	33
		Ir	190	95(1)	0.00(3)	· · ·	· · ·	Deicher *et al.*	34
		· · ·	· · ·	95	0	not ⟨110⟩	· · ·	Deicher *et al.*	27
		Ir	190	96(1)	0.45(3)	· · ·	· · ·	Deicher *et al.*	34
Cu	270	Im,Ir	400	49(1)	0	⟨111⟩	· · ·	Echt *et al.*; Wichert *et al.*	35–37
		Im	400	48(1)	0	⟨111⟩	· · ·	Arends	38
		Im	· · ·	52(2)	0.48(4)	· · ·	· · ·	Echt *et al.*; Wichert *et al.*	35,37
		Im,Ir,Q	250	109(1)	0	· · ·	· · ·	Echt *et al.*; Wichert *et al.*	35–37
		Im	(10)	111(2)	0	⟨110⟩	· · ·	Arends	38
		· · ·	· · ·	109	0	⟨110⟩	· · ·	Deicher *et al.*	27
		Im,Ir,Q	250	171(1)	0	· · ·	· · ·	Echt *et al.*; Wichert *et al.*	35–37
		Im	200	170(1)	0	· · ·	· · ·	Arends	38
		· · ·	· · ·	171	0	not ⟨110⟩	· · ·	Deicher *et al.*	27
Ni	400	Im	· · ·	· · ·	· · ·	· · ·	38(5)	Andreef *et al.*	39
		Im	350	<4	· · ·	· · ·	40(1)	Hohenemser *et al.*	15,40
		Ir	350	· · ·	· · ·	· · ·	40(1)	Suter *et al.*	41
		Im	· · ·	+32(2)	0	⟨111⟩	40(1)	Namavar *et al.*	42
		Im	270	53(5)	<0.2	⟨111⟩	39(5)	Hohenemser *et al.*	15–17
		Ir	· · ·	53(5)	· · ·	· · ·	· · ·	Suter *et al.*	41
Pd	350	Im	(20–400)	82(2)	0	· · ·	· · ·	Bertschat *et al.*	18,19
		Im	(10)	82(1)	0	⟨110⟩	· · ·	Butt *et al.*	43,44
		Im	(300)	82(2)	0	· · ·	· · ·	Müller	45
Pt	500	Im	300	58(8)	<0.2	· · ·	· · ·	Pleiter *et al.*	14
		Im,Ir	450	97(2)	0	· · ·	· · ·	Müller *et al.*	45–47
		Im	(10)	97(2)	<0.1	· · ·	· · ·	Pleiter *et al.*	14
		Im,Ir,Q	290	197(2)	0	· · ·	· · ·	Müller *et al.*	45–47
		Im	270	200(2)	<0.1	· · ·	· · ·	Pleiter *et al.*	14

[a] Temperatures given for stage III are approximate values derived from the resistivity literature (Ni: Ref. 49; Pd: Ref. 52; others: Ref. 48).

[b] The methods for introducing defects are abbreviated as follows: Im—implantation; Ir—irradiation; and Q—quenching. The column labeled T_{act} indicates temperatures at which defects were observed to be thermally activated. In the case of values enclosed in parentheses, the indicated temperature is an implantation temperature at which defects are observable directly following implantation, presumably through athermal activation.

[c] $\omega_0 = (3\pi/10)eQV_{zz}/h$ is the electric quadrupole frequency, η is the EFG asymmetry parameter, $\langle \cdots \rangle$ is the crystallographic direction along which the EFG principal z axis is oriented, and $\omega_L = \mu H_{hf}/hI$ is the magnetic Larmor frequency.

TABLE IV. Interpretation of observed defect sites.

Host	ω_0[a] (Mrad/s)	Activated in stage III?	Produced in quenching?	Activated in low-T implantation?	EFG symmetry $\langle \cdots \rangle$	η	Class[b]
Ag	34	Yes	Yes	No	· · ·	0	B
	75	Yes	No	Yes	⟨110⟩	0	A
Al	47	Yes	No	No	⟨111⟩	<0.2	B
	60	Yes	Yes	Yes	· · ·	0.41(2)	D
	124	Yes	Yes	Yes	⟨111⟩	<0.1	B
Au	38	Yes	Yes	No	⟨111⟩	0.00(3)	B
	86	Yes	Yes	Yes	⟨110⟩	0.00(3)	A
	95	Yes	No	No	not ⟨110⟩	0.00(3)	B
	96	Yes	No	No	· · ·	0.45(3)	D
Cu	49	Yes	No	No	⟨111⟩	0	B
	52	Yes	No	No	· · ·	0.48	D
	109	Yes	Yes	Yes	⟨110⟩	0	A
	171	Yes	Yes	No	not ⟨110⟩	0	B
Ni	< 4	Yes	· · ·	No	· · ·	· · ·	C
	53	Yes	· · ·	No	⟨111⟩	<0.2	B
Pd	82	No	No	Yes	⟨110⟩	0	A
Pt	58	Yes	No	No	· · ·	<0.2	B
	97	Yes	No	Yes	· · ·	<0.1	A
	197	Yes	Yes	No	· · ·	<0.1	B

[a] For definitions of ω_0, $\langle \cdots \rangle$, and η see Table III, footnote c.
[b] For definitions of classes A, B, C, and D, see text.

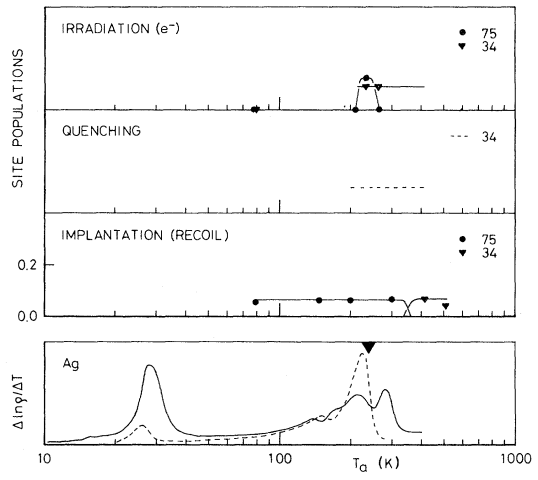

FIG. 7. Annealing behavior of defects in Ag, observed in PAC measurements on electron irradiated [Butt *et al.* (Ref. 25), Deicher *et al.* (Ref. 26)], quenched [Butt *et al.* (Ref. 25)], and implanted samples [Thomé and Bernas (Refs. 22–24)]. Defects are labeled by the corresponding quadrupole interaction frequencies. Also shown is the fractional change of the resistivity upon annealing after low-dose (Refs. 50,51) (bottom, drawn curve) and high-dose (Ref. 52) (bottom, broken curve) fast neutron irradiation. Stage III temperature according to Balluffi (Ref. 48) is marked (▼).

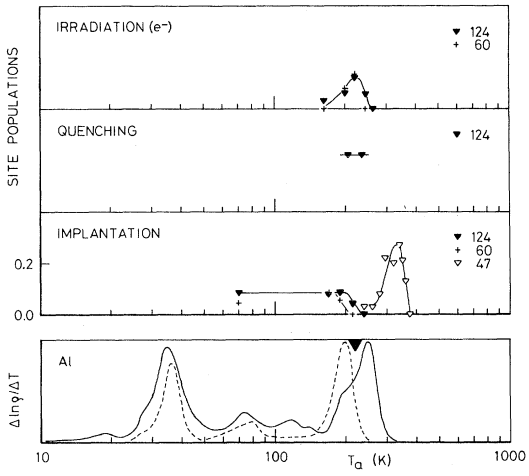

FIG. 8. Annealing behavior of defects in Al, observed in PAC measurements on electron irradiated [Rinneberg *et al.* (Ref. 28)], quenched [Rinneberg and Haas (Ref. 29)], and implanted samples (Pleiter and Prasad (Ref. 31)]. For further explanation, see caption of Fig. 7.

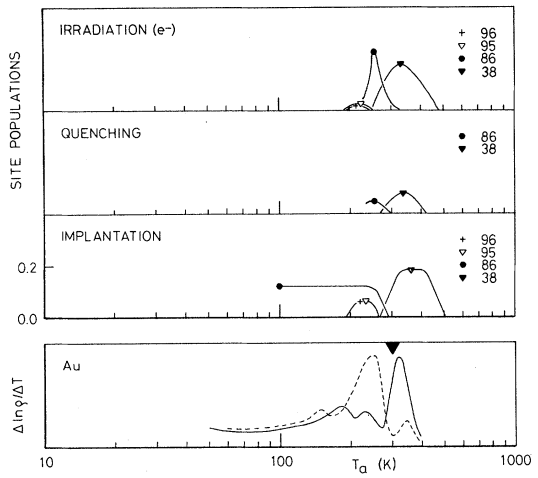

FIG. 9. Annealing behavior of defects in Au, observed in PAC measurements on electron irradiated [Deicher *et al.* (Ref. 34)], quenched [Deicher *et al.* (Ref. 34)] and implanted samples [Deicher *et al.* (Ref. 33)]. For further explanation, see caption of Fig. 7.

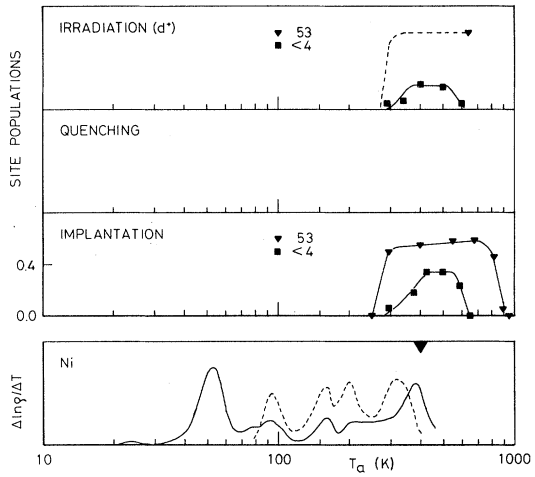

FIG. 11. Annealing behavior of defects in Ni, observed in PAC measurements on deuteron irradiated [Suter *et al.* (Ref. 41)], and implanted samples [Hohenemser *et al.* (Ref. 40)]. Quenching experiments have not been tried yet. Stage III temperature according to Ref. 49 is marked (▼). for further explanation, see caption of Fig. 7.

the result on Ag obtained by Behar *et al.*,[20,21] because it could not be reproduced by others in subsequent experiments, and the result on Ni obtained by Namavar *et al.*,[42] because it is based on an assumed unequal population of crystallographically equivalent defect states.

To indicate the annealing behavior of each of the observed frequencies for each method of state preparation, we have prepared summary plots for each of the metals, as shown in Figs. 7–13. For reference, the plots include annealing stages observed in resistivity experiments.[48–53]

In the following sections we interpret the data summarized in Table III. In doing so we employ general

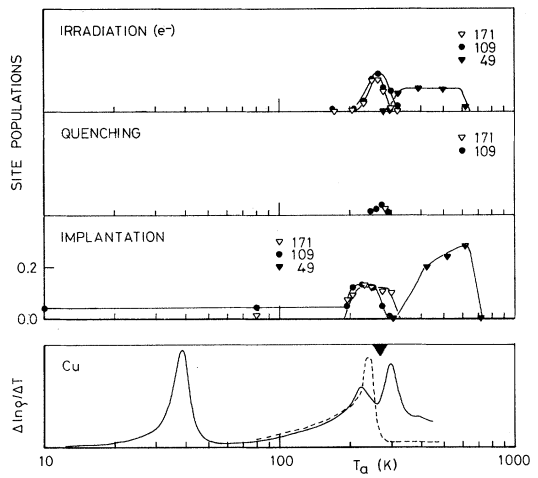

FIG. 10. Annealing behavior of defects in Cu, observed in PAC measurements on electron irradiated [Wichert *et al.* (Ref. 37)], quenched [Wichert *et al.* (Ref. 37)] and implanted samples [Echt *et al.* (Refs. 35,36), Arends (Ref. 38)]. For further explanation, see caption of Fig. 7.

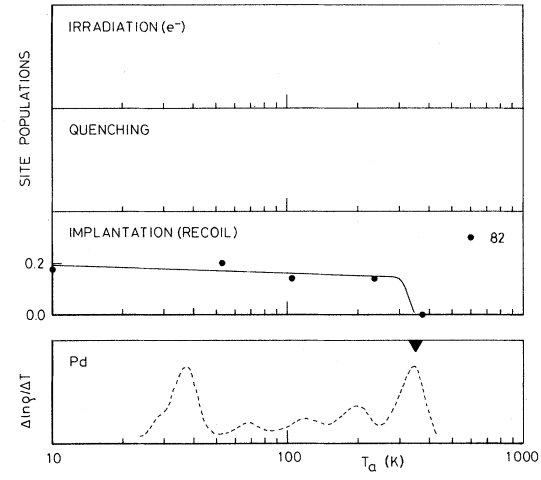

FIG. 12. Annealing behavior of defects in Pd, observed in PAC measurements on implanted samples [Butt *et al.* (Refs. 43,44), Müller (Ref. 45)]. No defects were observed after electron irradiation [Müller (Ref. 45)]. Quenching experiments have not been tried yet. Stage III temperature according to Ref. 52 is marked (▼). For further explanation, see caption of Fig. 7.

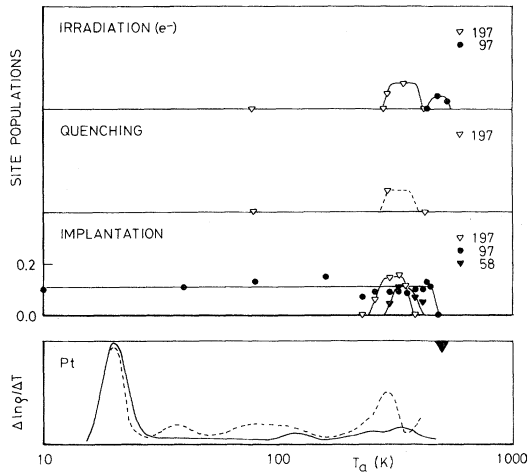

FIG. 13. Annealing behavior of defects in Pt, observed in PAC measurements on electron irradiated [Müller (Ref. 45)], quenched [Müller (Ref. 45)], and implanted samples [Pleiter *et al.* (Ref. 14), Müller and Krusch (Ref. 46)]. For further explanation, see caption of Fig. 7.

arguments based on classification and comparison of results obtained for various metals. We also draw freely on arguments made by the authors quoted in Table III. The reader who wishes to have further detail is encouraged to refer to the original publications.

VI. VACANCY CHARACTER OF THE DEFECTS

Several general arguments lead independently to the conclusion that the states observed consist largely of trapped vacancy defects. In the following we consider each of these arguments briefly. We present them in what we believe is a decreasing order of strength.

Association with stage III. Based on extensive experimental and theoretical evidence on fcc metals, stage III recovery is widely believed to involve free migration of vacancies or divacancies.[48] Therefore, the vacancy character of the observed defects may be established by demonstrating their association with stage III. As indicated in Table IV, all but 1 of the 19 sites observed in ^{111}In experiments on fcc metals are thermally activated in stage III. The only exception is the 81-Mrad/s state of Pd which occurs only as an athermally activated defect following low-temperature implantation of ^{111}In or ^{111}Pd, or in-beam recoil implantation of ^{111}Cd. In assigning stage III activation we admittedly use a rather broad definition of stage III, including for a given metal what may be several distinct substages. Evidence for this can be seen in Figs. 7–13, according to which various defects are activated at distinctly different temperatures in the stage III region.

Production through quenching. It is known for metals that vacancies are the only thermodynamically stable defect at high temperatures.[54] Hence, quenching from near the melting point is believed to produce a nonequilibrium distribution of frozen-in vacancies, but no other lattice defects. Thus the vacancy character of the observed defects may be directly established through quenching experiments. As shown in Table IV, of 17 possible cases for which quenching to below stage III has been tried (no data exist for Ni), there are eight cases for which the corresponding defect is subsequently activated in stage III. Nonobservation in the other nine cases may be due to the fact that quenching conditions were nonideal. It might also be that the defects involved are so large that they do not form in detectable concentration from the mono-vacancy densities that can be achieved in quenched samples.

Athermally activated trapping during low-temperature implantation. Energetic heavy ions slow down in a crystalline lattice via a series of replacement collisions. In such a sequence self-interstitials are transported away from the center of the damage cascade, leaving behind a depleted or vacancy rich region.[55] This region contains some close interstitial-vacancy pairs that recombine in stage I_A-I_D, plus a local vacancy concentration that may be as high as a few atomic percent.[56] From this picture it follows that any defects trapped athermally during low-temperature implantation must be vacancies from the depleted region. As shown in Table IV, seven of the 19 sites are formed in this way.

Impurity size effects. Elastic interactions between atoms may produce significant "impurity size effects." Thus, when impurity atoms are oversized vacancy binding will generally be large compared to interstitial binding; and when impurity atoms are small, the reverse is true.[23,57] As shown in Table V, the

TABLE V. Atomic radii of seven fcc metals and indium.

Element	Radius[a] (Å)
In	1.62
Ag	1.44
Al	1.43
Au	1.44
Cu	1.28
Ni	1.24
Pd	1.37
Pt	1.38

[a] Radius is half the nearest-neighbor distance in a crystal lattice, from Ref. 58.

^{111}In probe atoms are larger than all of the host atoms discussed here,[58] suggesting that vacancy trapping will predominate. Exceptions to this rule may arise when the electrostatic interaction between the impurity and vacancy produces zero or near-zero binding energy, e.g., when host and impurity atoms are iso-valent, or when the host valence is zero. (See below, Sec. VIII.) An example of the impurity size effect has recently been given by the Berlin group,[59] who observed that recoil-implanted ^{100}Pd (a small atom) traps defect only in stage I_E or the Nb host, whereas recoil implanted ^{111}In (a large atom) traps defects only in stage III.

Together our arguments strongly suggest a vacancy character for all 19 observed sites. Questions remain as to the geometric character of the various sites. Do they involve one, two, three, or many vacancies? What is their lattice location? To the extent it is possible, we discuss these questions next.

VII. CLASSIFICATION OF DEFECT STATES

As seen from Table IV, the observed defect sites may be characterized according to the frequency, method of production, and symmetry of the EFG. Using these variables we develop here a classification of states that leads to structural models in at least some cases. While our classification is fully developed here, it is in some respects comparable to parallel classification efforts applied by the Konstanz group to a more limited set of states.[26,27,60,61] A partial account of the present work was presented at the Darmstadt conference.[62]

EFG symmetry. With three notable exceptions, all vacancy states have an EFG with near-zero asymmetry parameter, η. This restricts possible geometries to configurations with at least a threefold axis of symmetry. For some cases measurements have been made on oriented single crystals, with the result that the crystallographic orientation of the EFG principal z axis is known. As indicated in Table IV, there are four cases which have the EFG principal z axis in the $\langle 110 \rangle$ crystallographic direction, and five others for which it points in the $\langle 111 \rangle$ direction. A special case is the single state in Ni which has a vanishing EFG, and hence cubic symmetry, but a magnetic hyperfine field that is only 40% of the value for ^{111}Cd in an undisturbed lattice position.

Single versus multiple traps. If irradiation, quenching, or implantation occurs under conditions which allow ample time for defect migration, complex multiple defect traps may form. However, if the temperature-of-state preparation or the time available for trapping prevents significant defect mobility, then any trap formed can involve only a single migrating species. Cases of such restricted mobility include states formed by ion implantation below stage III and all cases of in-beam recoil implantation. By inspection of Table IV we note that cases with the EFG principal z axis in the $\langle 110 \rangle$ crystallographic direction are *all* observed through athermal activation at low temperature. These defects are likely to be of simple structure. We note further, that the state with cubic symmetry and the states with the EFG principal z axis in the $\langle 111 \rangle$ direction, with one exception, are *never* observed through athermal activation at low temperature. These states, therefore, involve more than one defect.

This leads us to propose grouping of states into four classes, at least three of which permit a tentative assignment of structure. The definitions of these classes are as follows.

Class A. Defects are athermally activated during low-temperature implantation; $\eta = 0$; and the EFG principal z axis is oriented in the $\langle 110 \rangle$ crystallographic direction.

Class B. Defects are not athermally activated during low-temperature implantation or the EFG principal z axis is oriented in the $\langle 111 \rangle$ crystallographic direction; and $\eta = 0$.

Class C. Defects are not athermally activated during low-temperature implantation; and the EFG is near zero.

Class D. Defects have less than threefold symmetry, i.e., $\eta \neq 0$.

According to Table IV, Ag, Au, Cu, and Pd have one state each that satisfies all three criteria of class A, while Pt has one state that satisfies two of the three criteria of class A. We conjecture that all five cases are examples of class A. Defined in this way, class A exhibits a frequency distribution as shown in Fig. 14 (top). The close similarity of frequencies

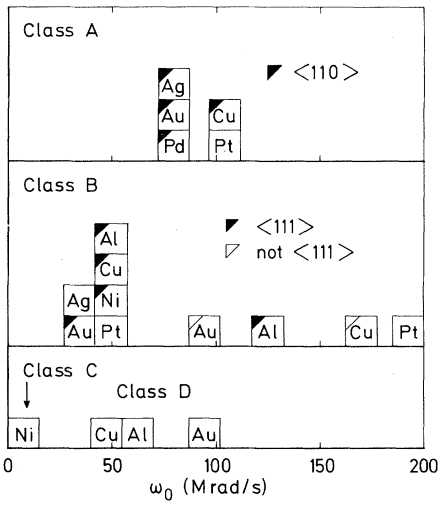

FIG. 14. Quadrupole frequency distribution of four classes of defects; $\langle \ldots \rangle$ is the crystallographic direction along which the EFG principal z axis is oriented.

suggests that a single-defect structure may be involved.

As shown in Table IV, each element except Pd has at least one class B state. Because Al, Au, Cu, and Pt have two class B states each, it is impossible that a single-defect structure is involved. However, the frequency distribution of states shown in Fig. 14 (middle), suggests that some of the sites with the EFG principal z axis in the $\langle 111 \rangle$ crystallographic direction may correspond to a single structure, and thus form a distinct subclass.

For class C the only known member is Ni. While similar structures probably exist in nonmagnetic fcc metals, they are likely to remain undetectable via PAC, for reasons already noted. The three defects of class D have nothing in common except a nonvanishing asymmetry parameter. For the present they must be considered a residual class which does not necessarily have a common structure. The frequency distribution for classes C and D are shown in Fig. 14 (bottom).

VIII. CLASS A: THE NEAREST-NEIGHBOR MONOVACANCY

The structural model we adopt for class A is simple and unambiguous. It may be expressed in terms of two propositions. (1) Since the vacancy trap is already formed during low-temperature irradiation, a single migrating species must be involved. (2) Since the $\langle 110 \rangle$ direction of the EFG principal z axis is the nearest-neighbor direction, a monovacancy in the nearest-neighbor position is most likely.

The observed interaction frequencies of class A sites range from 75 Mrad/s in Ag to 109 Mrad/s in Cu. A first-order understanding of these frequencies is based on a point-charge model of the EFG that neglects lattice relaxation

$$V_{zz}^{pc} = (4\pi\epsilon_0)^{-1}(1-\gamma_\infty)(2z_{eff}e/r_{NN}^3) \ . \tag{7}$$

Here $(1-\gamma_\infty)$ is the antishielding factor of the probe atom,[63] $z_{eff}e$ is the effective monovacancy charge, and r_{NN} is the nearest-neighbor distance. Using the observed values of the interaction frequencies, we calculated observed values of the EFG from the relation

$$|V_{zz}^{obs}| = (10/3\pi)(h/eQ)\omega_A^{obs} \ , \tag{8}$$

appropriate for the case of nuclear spin $I=\frac{5}{2}$ and $\eta=0$. From this and calculated values of V_{zz}^{pc} we obtain the ratio $|V_{zz}^{obs}/V_{zz}^{pc}|$. As shown in Table VI (top) this ratio ranges between 1.12 and 1.35 in the group Ag, Au, Cu, Pd, and Pt. This indicates that

TABLE VI. Electric field gradients of monovacancies in fcc metals.

Probe/Host	r_{NN} (Å)	ω_A^{obs} [a] (Mrad/s)	$\lvert V_{zz}^{obs}\rvert$ [b] (10^{21} V/m^2)	V_{zz}^{pc} [c] (10^{21} V/m^2)	$\lvert V_{zz}^{obs}/V_{zz}^{pc}\rvert = \lvert 1-K_A\rvert$
			^{111}Cd PAC experiments		
^{111}Cd/Ag	2.88	75	4.28	−3.65	1.17
^{111}Cd/Al	2.86	· · ·	· · ·	−11.19	· · ·
^{111}Cd/Au	2.88	86	4.90	−3.65	1.34
^{111}Cd/Cu	2.55	109	6.22	−5.26	1.18
^{111}Cd/Ni	2.49	· · ·	· · ·	−5.65	· · ·
^{111}Cd/Pd	2.75	82	4.68	−4.19	1.12
^{111}Cd/Pt	2.77	97	5.53	−4.10	1.35
			Host-atom NMR experiments		
^{27}Al/Al	2.86	1.38	0.40	−1.28	0.31
^{63}Cu/Cu	2.55	21.52	1.35	−3.19	0.42

[a] Values of ω_A^{obs} were directly taken from experiment, except the one for ^{27}Al/Al which was corrected for nonzero asymmetry parameter $\eta=0.65$.

[b] Values of V_{zz}^{obs} were calculated from Eq. (8) using the quadrupole moments $Q(^{111}\text{Cd})=0.77$ b, $Q(^{27}\text{Al})=0.15$ b, and $Q(^{63}\text{Cu})=-0.21$ b. In the case of ^{63}Cu/Cu, Eq. (8) has to be rewritten in a form appropriate for nuclear spin $I=\frac{3}{2}$.

[c] Values of V_{zz}^{pc} were calculated from Eq. (7) using $(1-\gamma_\infty)$ values given by Feiock and Johnson (Ref. 63) as follows: 30.27 for Cd^{++}, 18.37 for Cu^{+}, 3.46 for Al^{+++}; $z_{eff}=-3$ for Al and $z_{eff}=-1$ for all other cases; and values of r_{NN} as given above.

the point-charge model without lattice relaxation reproduces the observed gradients surprisingly well.

According to a parametrization of the EFG that has recently been extensively documented for dilute impurities in noncubic metals by Kaufmann and Vianden,[64] the observed EFG is the sum of a lattice contribution

$$V_{zz}^{\text{latt}} = (1-\gamma_\infty) \sum V_{zz}^{\text{ion}} \ , \tag{9}$$

and an electronic contribution

$$V_{zz}^{\text{el}} = V_{zz}^{\text{obs}} - V_{zz}^{\text{latt}} = -K V_{zz}^{\text{latt}} \ . \tag{10}$$

The proportionality constant K has been empirically determined through a comparison of a wide variety of noncubic metals, and found to be positive with a magnitude of about 2.5. For a nearest-neighbor monovacancy in an unrelaxed lattice, the lattice sum $\sum V_{zz}^{\text{ion}}$ may be replaced by $(4\pi\epsilon_0)^{-1}(2Z_{\text{eff}}e/r_{\text{NN}}^3)$ so that $V_{zz}^{\text{latt}} = V_{zz}^{\text{pc}}$. With this, the observed gradient takes the form

$$V_{zz}^{\text{obs}} = (1-K_A)(4\pi\epsilon_0)^{-1}(1-\gamma_\infty)(2Z_{\text{eff}}e/r_{\text{NN}}^3) \ , \tag{11}$$

and

$$|V_{zz}^{\text{obs}}/V_{zz}^{\text{pc}}| = |1-K_A| \ . \tag{12}$$

We assume that $K_A > 1$. This is in accord with EFG measurements for nearest-neighbor monovacancies made by Visser *et al.*[65] on I in Fe, and Reintsema *et al.*[66] on Cs in Mo. It also agrees with K values found by Kaufmann and Vianden[64] for impurities in noncubic metals. As shown in Table VI, our assumption leads to $2.12 \leq K_A \leq 2.35$ for the five monovacancy defects.

To demonstrate the similarity in EFG systematics, we compared the monovacancy data to the "universal" curve V_{zz}^{latt} vs V_{zz}^{el} found for impurities in noncubic metals by Raghavan *et al.*[67] As can be seen from Fig. 15, though the monovacancy results fall systematically below the curve of Raghavan *et al.*, there is reasonable agreement between the two sets of data. At the same time, as noted by Kaufmann and Vianden,[64] the existence of a universal curve should not be overinterpreted. Because of the strong correlation between V_{zz}^{latt} and V_{zz}^{el} that is built into this parametrization of the EFG, an experimental point will fall near the curve for a wide range of z_{eff} values. Existence of the universal curve requires only that the electronic enhancement factor K_a is positive, larger than one, and relatively constant from metal to metal.

The results of ^{111}Cd PAC experiments may be compared to the results obtained for host atoms by Minier *et al.*[68–70] Using NMR with field cycling, these authors found discrete resonance lines corresponding to field gradients $|V_{zz}| = 0.4 \times 10^{21}$ V/m^2 and 1.4×10^{21} V/m^2 for electron-irradiated Al and Cu, respectively. Assignment of the measured field

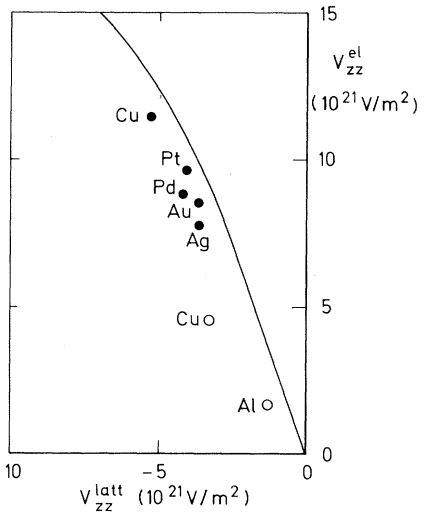

FIG. 15. Plot of V_{zz}^{latt} against V_{zz}^{el} for monovacancy sites in fcc metals. Solid circles: from PAC measurements using ^{111}Cd. Open circles: from NMR measurments on host atoms. Drawn line: "universal" curve found by Raghavan *et al.* (Ref. 67) for impurity atoms in noncubic metals.

gradients to monovacancies is made through a comparison with other lower frequency lines, presumed to correspond to more distant neighbor vacancies. In the case of Cu, vacancy trapping in stage III was also demonstrated.[70] As shown in Table VI (bottom), the ratio $|V_{zz}^{\text{obs}}/V_{zz}^{\text{pc}}|$ is approximately a factor of 3 lower for the host-atom NMR experiments than for ^{111}Cd PAC experiments.

Minier *et al.*[68] found $\eta = 0.65$ in the case of a nearest-neighbor monovacancy in Al. Similarly, large asymmetry parameters in the range 0.1–0.9 have been found at nearest neighbors of impurity atoms, by NMR on ^{27}Al in Al (Minier and Hodung,[71] Berthier and Minier [72]) and on ^{63,65}Cu in Cu (Jensen *et al.*,[73] Nevald,[74] Minier and Minier[69]), and by PAC on ^{100}Rh in the noble metals Cu, Ag, and Au (Królas *et al.*,[75] Arends[76]). For ^{111}Cd, in contrast, as already noted in Table IV, all class A defects give rise to $\eta \approx 0$. The same has been observed at nearest neighbors of impurity atoms (Królas *et al.*,[77,78] Baumvol *et al.*,[79] Arends[76]).

In this context it is interesting to note that a more sophisticated model of the EFG than that expressed by Eq. (11) accounts for the screening charge set up by the conduction electrons around the impurity atom. Langer and Vosko have treated the problem rigorously for a point charge in a free-electron gas by applying many-body perturbation theory.[80] Their asymptotic expression for the EFG has the form

$$V_{zz} \simeq A \cos(2k_F r + \varphi)/r^3 \ , \tag{13}$$

with k_F the Fermi wave number. Except near its ex-

trema, the variation of such a gradient is more rapid than $1/r^3$, and very sensitive to φ. This means that small differences in impurity-probe distance can produce large changes in V_{zz}^{obs}. We note further that the original Langer and Vosko theory gives a constant phase $\varphi = \pi$,[80] whereas values of φ ranging from 0 to about $\pi/2$ were derived from phase shifts of electron waves scattered by the impurity potential.[81–83] In addition, the Bloch character of the conduction electrons and the polarization of the electron cloud of the probe atom, which depends strongly on the form of the antishielding function $\gamma(r)$, leads to an enhancement of the EFG. In this light it is not unreasonable that measurements with different probe atoms yield different EFG results.

Taken together, our analysis of the class A defects in terms of monovacancies is, we believe, fairly robust. Yet as added confirmation, it would be worthwhile to test the analysis further by experimentally checking the following predictions. (1) There should exist a state in Al with interaction frequency $\omega_A \approx 230$ Mrad/s. This should occur in low-temperature implantation, and should be thermally activated following irradiation and quenching at a temperature of about 220 K. (2) There should exist a state in Ni with interaction frequency $\omega_A \approx 120$ Mrad/s. This should occur in low-temperature implantation, and should be thermally activated following irradiation and quenching at a temperature of about 400 K. (3) The class A states in Pd (82 Mrad/s) and Pt (97 Mrad/s), and the putative class A states in Al ($\approx$230 Mrad/s) and Ni ($\approx$120 Mrad/s) should all exhibit an EFG principal z axis oriented in the $\langle 110 \rangle$ crystallographic direction. (4) The class A states in Ag (75 Mrad/s), Pd (82 Mrad/s), and Pt (97 Mrad/s) should be observable in appropriately designed quenching experiments.

It is possible that the missing class A states in Al and Pd are related to the special nature of the electrostatic interaction in the two cases. Thus, the isovalent nature of the In^{+3}-Al^{+3} system may produce a near-zero impurity-vacancy binding energy. Similarly, the fact that Pd may have zero valence[84,85] can lead to near-zero electrostatic interaction between In atoms and Pd vacancies.

IX. MONOVACANCY MIGRATION AND BINDING ENTHALPIES

The assignment of the class A defect to the nearest-neighbor monovacancy enables us to calculate the monovacancy migration enthalpy, H_{1V}^m, and the In-vacancy binding enthalpy, $H_{\text{In-}V}^b$, from the annealing temperatures T_A and T_A' at which this defect is formed or disappears. In this section we apply rate theory to derive approximate values for these enthalpies from results of PAC measurements on electron-irradiated samples.

To simplify the problem, we shall neglect clustering and diffusion of vacancies, and assume that all vacancy sinks are insaturable. Under these conditions changes of defect concentrations with time are described by the following set of coupled equations[86]:

$$\dot{c}_{1V} = -Ac_{\text{In}}c_{1V} - \sum_i B_i c_i c_{1V} \ , \tag{14}$$

$$\dot{c}_A = +Ac_{\text{In}}c_{1V} \ , \tag{15}$$

where c_{1V}, c_{In}, c_i, c_A stand for the concentrations of monovacancies, In impurities, other insaturable sinks, and In-vacancy complexes. The reaction constant A is given by[86]

$$A = 84\nu \exp(-H_{1V}^m/kT_A) \ , \tag{16}$$

where ν is the Debye frequency for which we use values given in Ref. 54. The Eqs. (14) and (15) can be solved analytically, with result

$$c_{1V}(t) = c_{1V}(0)\exp(-\lambda t) \ , \tag{17}$$

$$c_A(t) = \lambda^{-1}Ac_{\text{In}}c_{1V}(0)[1-\exp(-\lambda t)]$$

$$= f_A c_{\text{In}}[1-\exp(-\lambda t)] \ , \tag{18}$$

$$\lambda = Ac_{\text{In}} + \sum_i B_i c_i \ . \tag{19}$$

Here, $c_{1V}(0)$ is the initial concentration of vacancies which follows from the reported Frenkel pair production assuming that 10 to 50% of the originally produced vacancies are still present at the onset of stage III; f_A is the observed fraction ^{111}In atoms that traps a class A defect; and λ^{-1} is the characteristic formation time of class A defects which is approximately equal to the reported annealing time, t_a. Thus, according to Eqs. (16) and (18) we have

$$H_{1V}^m = kT_A \ln[84\nu c_{1V}(0)t_a/f_A] \ . \tag{20}$$

In Table VII we give migration enthalpies that were calculated from Eq. (20) for cases in which thermally activated trapping of monovacancies has been observed. For Ni and Pd no monovacancy trapping has been found yet. However, for Pd we get an upper limit for the migration enthalpy from the detrapping temperature (see below). As shown in Fig. 16, the migration enthalpies derived from PAC experiments are slightly smaller than stage III migration enthalpies obtained from resistivity measurements.[48,49,87] This might reflect a lowering of the activation energy due to strain fields around the oversized In atom. It might also be attributed to the fact that Eq. (14) does not account for clustering and diffusion of vacancies.

The decay of class A defects is described by the equation[86]

$$\dot{c}_A = -A'c_A \tag{21}$$

TABLE VII. Monovacancy migration enthalpy, H^m_{1V}, and In—vacancy binding enthalpy, $H^b_{\text{In-}V}$.

Host	ν[a] (10^{12} Hz)	$c_{1V}(0)$[b] (ppm)	t_a[c] (10^2 s)	f_A[d]	Trapping[e] T_A (K)	Trapping[e] H^m_{1V} (eV)	Detrapping[e] T'_A (K)	Detrapping[e] $H^m_{1V}+H^b_{\text{In-}V}$ (eV)	References
Ag	2.16	60–300	6	0.12	220	0.62	250	0.81	25
Au	1.61	60–300	6	0.24	240	0.65	270	0.86	34
Cu	3.47	10–40	6	0.12	260	0.69	290	0.95	37
		60–300	6	0.13	240	0.68	290	0.95	37
Pd	(2)	· · ·	18	· · ·	· · ·	<1.16	340	1.13	45
Pt	2.10	≈200	18	0.05	450	1.31	530	1.76	45
		· · ·	9	· · ·	· · ·	· · ·	470	1.53	14

[a] Debye frequency for Pd is estimated, others from Ref. 54.
[b] Initial vacancy concentration calculated from reported Frenkel pair production, assuming that 10% to 50% of the originally produced vacancies survive preceding annealing stages.
[c] Reported annealing time.
[d] Fraction of ^{111}In atoms involved in class A defect formation, directly taken from experiment.
[e] Uncertainty in reported values of trapping and detrapping temperatures is typically 10 K; uncertainty in derived values of migration and binding enthalpies is 0.03–0.04 eV.

with the reaction constant[86]

$$A' = 14\nu' \exp[-(H^m_{1V} + H^b_{\text{In-}V})/kT'_A] \quad . \tag{22}$$

Since detrapping requires only a single jump, we have $t_a = A'^{-1}$ and

$$H^m_{1V} + H^b_{\text{In-}V} = kT'_A \ln(14\nu' t_a) \quad . \tag{23}$$

In Table VII we give the sum of migration and binding enthalpies that were derived from Eq. (23), assuming $\nu' = \nu$. The binding enthalpies have the remarkably constant value $H^b_{\text{In-}V} \approx 0.2$ eV. This somewhat unexpected result is in contradiction with predictions made from several theoretical models.[57]

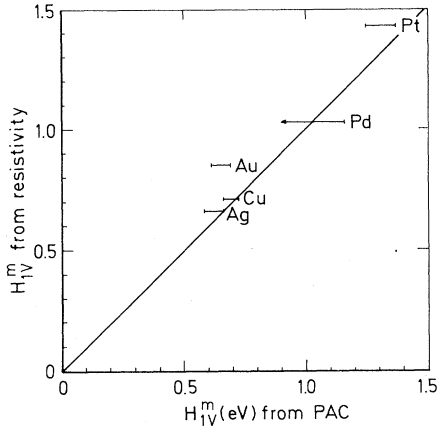

FIG. 16. Plot of the monovacancy migration enthalpy H^m_{1V} derived from PAC measurements against the corresponding value obtained in resistivity experiments (Pd: from Ref. 84; others: from Ref. 48).

X. CLASS B: DIVACANCIES OR FAULTED LOOPS IN THE {111} PLANE

As defined in Sec. VII, class B shows a wide dispersion of observed quadrupole frequencies. The structural model adopted for these states must therefore leave room for several distinct forms. Given the identification of the nearest-neighbor monovacancy as proposed in Sec. VIII, an effective way of analyzing for possible single-structure subclasses of class B is to form the ratio between the observed class B and class A quadrupole interaction frequencies. As displayed in Table VIII, this shows that six of nine class B states cluster in a narrow range around $\omega_B/\omega_A \approx 0.5$, while four other states are removed by a factor of 2 or more. Four of the six states with $\omega_B/\omega_A \approx 0.5$ have an EFG principal z axis oriented in the ⟨111⟩ crystallographic direction. We therefore hypothesize that a single structure is involved in all six states, and in further discussion identify these as subclass B_1. Because of widely varying ω_B/ω_A and the absence of other structural information we identify the remaining four states as a residual subclass, B_x, that may prove to include several distinct structures.

We may show for both subclasses that they involve defects in which two or more vacancies are trapped. For subclass B_1 there are four independent arguments. (1) To obtain an EFG with principal z axis directed in the ⟨111⟩ crystallographic direction, a minimum of two vacancies is required, as argued by Hohenemser *et al.*[15] (2) In the case of Ni the 53-Mrad/s defect is associated with a magnetic hyperfine field that is only 40% of the field for ^{111}In in an undisturbed Ni lattice.[15] Such a large reduction in hy-

TABLE VIII. Analysis of class B into subclasses.

Host	ω_0 (Mrad/s)	ω_B/ω_A	Direction of EFG principal z axis	Subclass identification
Al	124	(0.54)[a]	⟨111⟩	B_1
Ag	34	0.45	· · ·	
Au	38	0.44	⟨111⟩	
Cu	49	0.45	⟨111⟩	
Ni	53	(0.44)[b]	⟨111⟩	
Pt	58	0.60	· · ·	
Al	47	(0.20)[a]	⟨111⟩	B_x
Au	95	1.10	not ⟨111⟩[c]	
Cu	171	1.57	not ⟨111⟩[c]	
Pt	197	2.03	· · ·	

[a] Assumes existence of a 230 Mrad/s class A state for Al.
[b] Assumes existence of a 120 Mrad/s class A state for Ni.
[c] Conclusion drawn by present authors.

perfine field is not expected theoretically for monovacancies, nor has it been observed in cases that could be assigned as trapped monovacancies with reasonable confidence.[65,66] Hence, the 53-Mrad/s state must involve more than one vacancy. (3) For Ni the 53-Mrad/s state is activated in a narrow range of temperatures around 270 K, and the same holds for the subclass B_1 states in Al and Pt. In the cases of Ni and Pt the trapping temperatures correspond with divacancy migration according to resistivity literature.[48,49] (4) For Cu and Au activation of subclass B_1 is not sharply defined, and observed at temperatures that differ distinctly from those we have identified with class A defects (see Figs. 7–13). This suggests that these defects are formed through multiple trapping of vacancies.

For subclass B_x there is an additional argument indicating that more than one vacancy is trapped: in three cases where the EFG is significantly larger than the EFG we have identified with nearest-neighbor monovacancies. If it can be assumed that a single vacancy cannot produce a larger EFG than it produces in a nearest-neighbor position, then these subclass B_x defects involve at least divacancies.

At least two specific structural models have been proposed to explain specific examples of what we have called subclass B_1 defects. In considering the defects in Cu and Au Echt *et al.*[36] and Deicher *et al.*[34] have suggested faulted loops in the {111} plane, with the In in an interstitial site [Fig. 17(a)]. This model of subclass B_1 in effect involves a defect of indefinite size, yet well-defined EFG with principal z axis in the ⟨111⟩ crystallographic direction. However, in the case of maximum relaxation of the planes neighboring the fault the lattice-constant ratio of the local hcp structure takes the ideal value $c/a = (\frac{8}{3})^{1/2}$ for which the magnitude of V_{zz} approaches zero.[64]

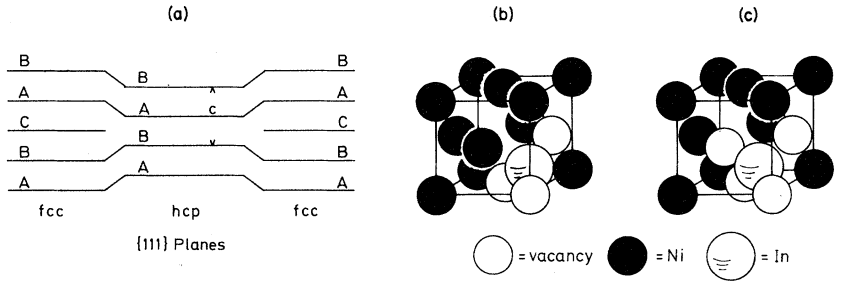

FIG. 17. Lattice models of subclass B_1 and class C defects. (a) Faulted loop suggested by the Konstanz group (Ref. 27). (b) Interstitial In atom at the center of a 60° trivacancy. (c) Interstitial In atom at the center of a tetrahedron consisting of four nearest-neighbor vacancies.

In contrast, when discussing the case of Ni, we and our colleagues in Groningen[15,17] have assumed trapping of a divacancy in two adjacent face-center sites with relaxation of the In atom from its cube corner position to an interstitial site located at the center of an equilateral triangle in the {111} plane [Fig. 17(b)].

Which model, if either, is correct? An argument for the Konstanz faulted loop model is that for Cu and Au the defect breaks up over a range of annealing temperatures, depending on the dose, and particle type used in irradiation.[34,36] This suggests that the defect has varying degrees of stability which could be brought about by varying defect size. An argument of our own simple divacancy model is that with the exception of Cu and Au, subclass B_1 defects show sharp, well-defined trapping behavior suggestive of capture of a single, migrating species; and that at least in the case of Ni and Pt the trapping temperature has been independently associated with divacancy migration.[48,49] It is, of course, possible that both models are right, i.e., that the defect starts out as a simple divacancy trap, and then grows to an indefinite size without significantly changing its interaction frequency or EFG orientation. But that seems at least somewhat implausible.

A key to further validation of either of the models for subclass B_1 defects would be verification that In impurities are indeed in interstitial locations. This can, in principle, be demonstrated via channeling experiments on single crystals that contain the desired defect state in sufficient concentration. So far, unfortunately, relevant channeling experiments have led to apparently conflicting results, as follows. (1) In Al containing 0.02 at.% In or Sn, strong flux peaking effects have been seen by Swanson *et al.*,[88] suggesting that at least part of the impurities occupy interstitial positions. (2) Results of channeling experiments on Ni implanted with Bi obtained by Callaghan *et al.*[89] indicate that about half of the Bi atoms are close to dislocations in the {111} plane, and are shifted over a range of distances along the Burgers vector $\frac{1}{3}\langle 111\rangle$; this supports the Konstanz faulted loop model. (3) In contrast to these results, channeling experiments performed by Arends *et al.*[90] on Ni implanted with In recently showed that nearly all impurity atoms were close to regular lattice sites, with the implication that none of the interstitial models is correct.

We believe the apparently contradictory character of the channeling results reflects as much the uncertainty of that technique as the structure of the lattice defects studied. It is by no means impossible that at the implantation dose of 4×10^{14} at./cm^2 or more required for the In*Ni* work,[90] the implantation itself strongly disturbs the defect structure. This ambiguity can only be avoided by doing channeling experiments on the same samples as used in PAC work—a combination that has for a variety of reasons not been achieved so far.

Finally, we should not restrict our discussion to planar defects, but also consider three-dimensional defect structures like voids. Indeed, it has been shown by small-angle scattering of neutrons from Al that there exist octahedral voids bounded by {111} faces.[91] An In atom adsorbed on such a free internal surface will experience an EFG with hexagonal symmetry. This would be a third model that would account for all the class B defect properties. For that reason, it should not be ruled out beforehand, although its applicability is limited to those states for which void formation occurs above stage III.

It remains to see if the frequencies for subclass B_1 can be understood. To do so it is tempting to adopt the same parametrization as in the case of class A, and write

$$\omega_B^{\rm obs}/\omega_B^{\rm pc}=|1-K_B| \quad . \tag{24}$$

However, calculation of $\omega_B^{\rm pc}$ leads to difficulties of two kinds. (1) There is no unique defect configuration as in class A, and one has therefore to deal with a range of configurations involving various numbers of vacancies. (2) For two or more vacancies around an In site, substantial lattice relaxation can be expected, with the result that a rigid-lattice lattice sum will not yield quantitatively correct EFGs. It is therefore impossible to calculate $\omega_B^{\rm pc}$ in a reliable way, and to extract from this a value of $|1-K_B|$.

Our conclusion about the structure of subclass B_1 must therefore remain somewhat ambiguous. On the one hand we feel sure that a relatively simple defect, most probably a divacancy, is trapped to form a state with the EFG principal z axis in the $\langle 111\rangle$ crystallographic direction. Under certain conditions this initial state may grow into a larger defect in the {111} plane without significant change in the local EFG. On the other hand, we cannot decide whether the probe atom is interstitial or substitutional; nor can we explain the observed interaction frequencies in a quantitative manner, as for class A.

This emerging picture of subclass B_1 provides several predictions which ought to be tested in further experimental work, as follows. (1) There should exist a state in Pd with interaction frequency $\omega_B\simeq 40$ Mrad/s. (2) The putative state in Pd ($\approx$40 Mrad/s), as well as the B_1 states in Ag (34 Mrad/s) and Pt (58 Mrad/s) should all exhibit an EFG with principal z axis oriented in the $\langle 111\rangle$ direction. (3) If the Konstanz model of an extended planar defect is generally applicable, it ought to be possible to observe dose dependence and irradiating particle dependence of the breakup temperature for the subclass B_1 states in Al, Ag, Ni, Pd, and Pt.

XI. CLASS C: THE ZERO EFG SITE

The structural model for the class C defect, like that for class B, is not unique and unambiguous.

Common to any model, however, is the assumption that two or more vacancies are involved. The most striking feature to be explained is the fact that the defect has both a near-zero EFG and a well-defined magnetic hyperfine field, showing a distribution of less than 2% (Hohenemser *et al.*[15]). The sharply defined magnetic hyperfine field suggests that the defect involves a single, and probably unique structure. The vanishing EFG can arise in two fundamentally different ways. (1) The defect may have cubic symmetry, with the result that both the lattice and electronic contributions to the EFG are zero. (2) The defect may have noncubic symmetry, but be of the right size so that the lattice and electronic contributions to the EFG are equal and opposite in sign [recall Eq. (10)].

Interestingly, these two possibilities have somewhat different implications for nonmagnetic fcc metals. In the case of true cubic symmetry, class C should be strictly unobservable by PAC for all metals; while for equal but opposite lattice and electronic contributions, the class should be observed in at least some cases, since the enhancement factor, K, and effective charge, z_{eff}, will surely vary somewhat from metal to metal. Because no low-frequency states with appropriate annealing characteristics have been observed in nonmagnetic fcc metals we believe there is good reason to assign true cubic symmetry to the class C state.

The simplest configuration having true cubic symmetry is an In atom at the center of a tetrahedron consisting of four nearest-neighbor vacancies [see Fig. 17(c)]. This three-dimensional cluster which was proposed by Hohenemser *et al.*[15] requires an interstitial position for the In atom, as in the case of class B_1. The cubic symmetry of this site is expected to be conserved even if lattice relaxation occurs.

Recent positron annihilation studies by Dlubek *et al.*[92] support this model in a general way, i.e., they give evidence of three-dimensional clustering around Sb impurities in Ni with a temperature dependence that closely follows the observed annealing behavior of the class C defect in Ni. Similar clustering of vacancies around interstitial In and Sn impurities in Al has been deduced in channeling experiments already mentioned.[88] Dlubek *et al.* interpret their data to involve microvoids that grow to an eventual size of 100 or more vacancies per site. It is not possible that the class C site in Ni has the character of such microvoids. If the vacancy cluster should grow beyond the tetrahedral configuration shown in Fig. 17(c), both the cubic symmetry and the homogeneity of the hyperfine field will be destroyed. The class C defect must therefore involve a very specific subset of population of microvoids.

Evidence that this is so may be derived from experiments in which the dose is varied. Data on implanted (Arends[38]), deuteron-bombarded (Suter *et al.*[41]), and cold-worked (Collins *et al.*[93]) samples of ^{111}In*Ni* all show that trapping of the class C defect first increases with increasing dose, but then goes to zero when damage concentration becomes sufficiently high. This suggests that the defect is of limited size, and that it is destroyed when high vacancy concentration makes the formation of larger clusters more likely.

XII. SUMMARY AND CONCLUSIONS

Our comparative survey and interpretation of defect migration, trapping, and clustering near stage III in fcc metals has yielded a number of results on defect structure, as follows. (1) The PAC and PAD techniques provide a unique set of spectroscopic labels for a range of defect structures. (2) For a variety of independent reasons all of the defects observed to trap near stage III appear to be of the vacancy type. (3) Thirteen of the nineteen defect states surveyed have been observed via two or more methods of defect production, indicating that the observed structures are not dependent of the method of production. (4) For a set of similar metals, such as the seven fcc metals we have considered here, the observed spectroscopic states appear to fall into distinct classes. (5) For three of the classes or subclasses we have identified, reasonably well-supported structural models are proposed. For the nearest-neighbor monovacancy the structural model is sufficiently detailed to permit a unique, quantitative interpretation of the observed signals. For the vacancy defects with ⟨111⟩ and cubic symmetry the structural models are more suggestive than conclusive.

In short, our comparative analysis demonstrates that we are well on the way to understanding the structure of some single and multivacancy traps in fcc metals. To further test the generality of these conclusions it would be useful to conduct a number of additional experiments, as follows.

Test of the systematics. To check the proposed systematics it would be interesting to fill the gaps in Table IV in those cases for which classes are related to particular structural models. Specific objects of study would be cases where, for a given class, a defect is missing, or where an observed defect is only tentatively assigned to a class. In this spirit, the following interesting questions should be solved in further experiments.

Does a class A defect (monovacancy) exist for Al and Ni? Can the ⟨110⟩ symmetry of the 97-Mrad/s state in Pt be demonstrated?

Does a class B defect (divacancy or faulted-loop) exist for Pd? Can the ⟨111⟩ symmetry of the 34-Mrad/s state in Ag and the 58-Mrad/s state in Pt be demonstrated?

Can the class C defect (cubic symmetry) be identified in the case of nonmagnetic metals?

Expanding the structural analysis. A second ap-

proach to further work on structural systematics concerns defects for which no model has been suggested. These include the residual states for class C, for which $\eta = 0$, and all of class D, for which $\eta \neq 0$. Here some interesting questions are: Do corresponding states exist for all seven metals? What structures are involved in these states?

Other methods of defect production. A third approach to testing the systematics involves methods of defect production other than the three (irradiation, implantation, and quenching) that we have surveyed. So far, information on other methods is rather fragmentary, though recent work shows promise. for example, Collins[93] and Müller[94] have each done experiments which employ cold working to introduce defects. Similarly, Pleiter and Prasad[95] have introduced defects via laser quenching. Though each of these experiments has a number of interesting aspects in its own right, the overall conclusion seems to be that no new defects are seen. In further systematic work it would be worthwhile to check this tentative conclusion.

Beyond systematics of defect structure one would like to know about pathways by which various multivacancy structures are formed from migrating elementary defects. If PAC and PAD spectroscopy is to serve as a useful link between point-defect studies and the study of large aggregates that are seen via electron microscopy, it is essential that work on transformation rules and formation pathways be begun. From an experimental point of view this demands careful attention to the concentration of elementary defects and trapping impurities, as well as the details of annealing behavior. Because few of the experiments surveyed provide such information, what is needed are "second generation" studies that specifically address the details of transformation processes.

ACKNOWLEDGMENTS

The authors wish to thank Arend Arends, Gary Collins, and Hanny Diemer for a number of helpful discussions throughout the course of this work. Research at the University of Groningen was partly financed by the Stichting voor Fundamenteel Onderzoek der Materie (F.O.M) subsidized through the Nederlandse Organisatie voor Zuiver Wetenschappelijk Onderzoek (Z.W.O.). Research at Clark University was supported in part by the National Science Foundation, Grant No. DMR 80-02443.

[1] *Vacancies and Interstitials in Metals,* edited by A. Seeger, D. Schumacher, W. Schilling, and J. Diehl (North-Holland, Amsterdam, 1970).
[2] *Fundamental Aspects of Radiation Damage in Metals,* edited by M. T. Robinson and F. W. Young (U.S. Department of Commerce, Springfield, VA, 1976).
[3] *Properties of Atomic Defects in Metals,* edited by N. L. Peterson and R. W. Siegel (North-Holland, Amsterdam, 1978).
[4] *Radiation Induced Voids in Metals,* edited by J. W. Corbett and L. C. Ianello (U.S. Atomic Energy Commission, Oak Ridge, Tenn., 1972).
[5] *The Physics of Irradiation Produced Voids,* edited by R. S. Nelson (U.K. Atomic Energy Authority, Harwell, United Kingdom, 1975).
[6] W. Schilling and K. Sonnenberg, J. Phys. F 3, 322 (1973).
[7] W. Schilling, Hyper. Inter. 4, 636 (1978).
[8] P. Haasen, *Physical Metallurgy* (Cambridge University, Cambridge, United Kingdom, 1978), p. 220.
[9] F. W. Young, in Ref. 3, p. 310, and references therein.
[10] *Site Characterization and Aggregation of Implanted Atoms in Materials,* edited by A. Perez and R. Coussement (Plenum, New York, 1980).
[11] *The Electromagnetic Interaction in Nuclear Spectroscopy,* edited by W. D. Hamilton (North-Holland, Amsterdam, 1975).
[12] H. Frauenfelder and R. M. Steffen, in *Alpha-, Beta-, and Gamma-Ray Spectroscopy,* edited by K. Siegbahn (North-Holland, Amsterdam, 1968).
[13] B. Harmatz, Nucl. Data Sheets 27, 453 (1975).
[14] F. Pleiter, W. Z. Venema and A. R. Arends, Hyper. Inter. 4, 693 (1978).
[15] C. Hohenemser, A. R. Arends, H. de Waard, H. G. Devare, F. Pleiter, and S. A. Drentje, Hyper. Inter. 3, 297 (1977).
[16] F. Pleiter, A. R. Arends, and H. G. Devare, Hyper. Inter. 3, 87 (1977).
[17] F. Pleiter, Hyper. Inter. 5, 109 (1977).
[18] H. Bertschat, H. Haas, F. Pleiter, E. Recknagel, E. Schlodder, and B. Spellmeyer, Phys. Rev. B 12, 1 (1975).
[19] H. Bertschat, O. Echt, H. Haas, E. Ivanov, F. Pleiter, E. Recknagel, E. Schlodder, and B. Spellmeyer, Hyper. Inter. 2, 339 (1976).
[20] M. Behar and R. M. Steffen, Phys. Rev. Lett. 29, 116 (1972).
[21] M. Behar and R. M. Steffen, Phys. Rev. C 7, 788 (1973).
[22] L. Thomé and H. Bernas, Phys. Rev. Lett. 36, 1055 (1976).
[23] L. Thomé and H. Bernas, Hyper. Inter. 5, 361 (1978).
[24] L. Thomé, thesis (Université de Paris-Sud, Orsay, 1978) (unpublished).
[25] R. Butt, R. Keitel, and G. Vogl, in *Annual Report 1978* (Hahn-Meitner-Institut, Berlin-West, 1979), p. 68.
[26] M. Deicher, E. Recknagel, and Th. Wichert, Hyper. Inter. 10, 675 (1981).
[27] M. Deicher, O. Echt, E. Recknagel, and Th. Wichert, in *Nuclear and Electron Resonance Spectroscopies Applied to Materials Science,* edited by E. N. Kaufmann and G. K. Shenoy (North-Holland, Amsterdam, 1981), p. 435.
[28] H. Rinneberg, W. Semmler, and G. Antesberger, Phys. Lett. A 66, 57 (1978).
[29] H. Rinneberg and H. Haas, Hyper. Inter. 4, 678 (1978).
[30] H. Haas (private communication).

[31]F. Pleiter and K. G. Prasad (unpublished).
[32]H. G. Müller, unpublished results.
[33]M. Deicher, E. Recknagel, and Th. Wichert, in *Annual Report 1978* (University of Konstanz, Nukleare Festkörperphysik, Konstanz, 1979), p. 14.
[34]M. Deicher, E. Recknagel, and Th. Wichert, Radiat. Eff. 54, 155 (1981).
[35]O. Echt, E. Recknagel, A. Weidinger, and Th. Wichert, Hyper. Inter. 4, 706 (1978).
[36]O. Echt, E. Recknagel, A. Weidinger, and Th. Wichert, Z. Phys. B 32, 59 (1978).
[37]Th. Wichert, M. Deicher, O. Echt, and E. Recknagel, Phys. Rev. Lett. 41, 1659 (1978).
[38]A. R. Arends, unpublished results.
[39]A. Andreff, H.-J. Hunger, and S. Unterricker, in *Hyperfine Interactions Studied in Nuclear Reactions and Decay, Contributed Papers,* edited by E. Karlsson and R. Wäppling (University of Uppsala, Uppsala, 1974), p. 68.
[40]C. Hohenemser, A. R. Arends, and H. de Waard, Phys. Rev. B 11, 4522 (1975).
[41]R. M. Suter, M. Haoui, and C. Hohenemser, Hyper. Inter. 4, 711 (1978).
[42]F. Namavar, M. Rots, R. Coussement, H. Ooms, and J. Cales, Hyper. Inter. 4, 716 (1978).
[43]R. Butt, H. Haas, T. Butz, W. Mansel, and A. Vasquez, Phys. Lett. A 64, 309 (1977).
[44]R. Butt, thesis (Freie Universität, Berlin-West, 1977) (unpublished).
[45]H. G. Müller, thesis (University of Bonn, Bonn, 1979) (unpublished).
[46]H. G. Müller, K. Krien, and E. Bodenstedt, Phys. Rev. B 14, 5165 (1976).
[47]H. G. Müller and K. Krusch, Hyper. Inter. 4, 687 (1978).
[48]R. W. Balluffi, in Ref. 3, p. 240.
[49]W. Wycisk and M. Feller-Kniepmeier, in Ref. 3, p. 616.
[50]G. Burger, thesis (Technische Hochschule, Munich, 1965) (unpublished).
[51]G. Burger, K. Isebeck, J. Völkl, W. Schilling, and H. Wenzl, Z. Angew. Phys. 22, 452 (1967).
[52]M. Nakagawa, K. Bönig, P. Rosner, and G. Vogl, Phys. Rev. B 16, 5285 (1977).
[53]E. A. Ryan, Y. N. Lwin, J. J. Jackson, and D. L. Emerson, Radiat. Eff. 24, 89, (1975).
[54]A. Seeger and H. Mehrer, in Ref. 1, p. 1.
[55]A. Seeger, in *Radiation Damage in Solids* (I.A.E.A., Vienna, 1962), Vol. I, p. 101.
[56]H. Bernas, Phys. Scr. 11, 167 (1975).
[57]M. Doyama, in Ref. 3, p. 350.
[58]W. B. Pearson, *A Handbook of Lattice Spacings and Structures of Metals and Alloys* (Pergamon, London, 1958), p. 123ff.
[59]R. Sieleman, H. Metzner, S. Klaumünzer, R. Butt, H. Haas, and G. Vogl, Hyper. Inter. 10, 701 (1981).
[60]M. Deicher, O. Echt, E. Recknagel, and Th. Wichert, Hyper. Inter. 10, 667 (1981).
[61]Th. Wichert and E. Recknagel, in Ref. 27, p. 211.
[62]F. Pleiter, in *Nuclear Physics Methods in Materials Research,* edited by K. Bethge, H. Baumann, H. Jex, and F. Rauch (Vieweg, Braunschweig, 1980), p. 174.
[63]F. D. Feiock and W. R. Johnson, Phys. Rev. 187, 39 (1969).
[64]E. N. Kaufmann and R. J. Vianden, Rev. Mod. Phys. 51, 161 (1979).
[65]D. Visser, L. Niesen, H. Postma, and H. de Waard, Phys. Lett. 41, 882 (1978).
[66]S. R. Reintsema, E. Verbiest, J. Odeurs, and H. Pattyn, J. Phys. F 9, 1511 (1979).
[67]R. S. Raghavan, E. N. Kaufmann, and P. Raghavan, Phys. Rev. Lett. 34, 1280 (1975).
[68]M. Minier, R. Adreani, and C. Minier, Phys. Rev. B 18, 102 (1978).
[69]M. Minier and C. Minier, Phys. Rev. B 22, 21 (1980).
[70]C. Minier, M. Minier, and R. Adreani, Phys. Rev. B 22, 28 (1980).
[71]M. Minier and S. Hodung, J. Phys. F 7, 503 (1977).
[72]C. Berthier and M. Minier, J. Phys. F 7, 515 (1977).
[73]B. L. Jensen, R. Nevald, and D. L. L. Williams, J. Phys. F 2, 169 (1972).
[74]R. Nevald, J. Phys. F 5, L1810 (1975).
[75]K. Królas, P. Heubes, G. Schatz, and A. Weidinger, Hyper. Inter. 9, 297 (1981).
[76]A. R. Arends (unpublished).
[77]K. Królas, B. Wodniecka, and P. Wodniecki, Hyper. Inter. 4, 605 (1978).
[78]K. Królas, in *Hyperfine Interactions,* edited by R. Kulessa and K. Królas (Jagiellonian University, Kraków, Poland, 1979).
[79]I. J. R. Baumvol, M. Behar, J. A. H. da Jornada, R. P. Livi, K. W. Lodge, A. Lopez Garcia, and F. C. Zawislak, Phys. Rev. B 22, 5115 (1980).
[80]J. S. Langer and S. H. Vosko, J. Phys. Chem. Solids 12, 196 (1959).
[81]A. Blandin and J. Friedel, J. Phys. Radium 21, 689 (1960).
[82]W. Kohn and S. H. Vosko, Phys. Rev. 119, 912 (1960).
[83]P. L. Sagalyn and M. N. Alexander, Phys. Rev. B 15, 5581 (1977).
[84]J. B. Darby, Jr., K. M. Myles, and J. N. Pratt, Acta Metall. 19, 7 (1971).
[85]D. J. Lam and K. M. Myles, J. Phys. Soc. Jpn. 21, 1503 (1966).
[86]J. S. Koehler, in Ref. 1, p. 169.
[87]W. Köster and H. P. Kehrer, Z. Metallkd. 56, 760 (1965).
[88]M. L. Swanson, L. M. Howe, and A. F. Quenneville, Phys. Rev. B 22, 2213 (1980).
[89]P. T. Callaghan, P. Kittel, N. J. Stone, and P. D. Johnston, Phys. Rev. B 14, 3722 (1976).
[90]A. R. Arends, H. Hasper, C. Hohenemser, J. G. Mullen, G. van Opbroek, and F. Pleiter, Hyper. Inter. 10, 659 (1981).
[91]R. W. Hendricks, J. Schelten, and G. Lippman, Philos. Mag. 36, 907 (1977).
[92]G. Dlubek, O. Brümmer, N. Meyendorff, P. Hautojärvi, A. Vehanen, and J. Yli-Kauppila, J. Phys. F 9, 1961 (1979).
[93]G. S. Collins, G. Stern, and C. Hohenemser, Phys. Lett. 84A, 239 (1981).
[94]H. G. Müller, in Ref. 62, p. 418.
[95]F. Pleiter and K. G. Prasad, Phys. Lett. 84A, 345 (1981).